Physical Modeling of Fluid Flow in Ladles of Aluminum Equipped with Impeller and Gas Purging For Degassing

EUDOXIO RAMOS GÓMEZ, ROBERTO ZENIT, CARLOS GONZÁLEZ RIVERA, GERARDO TRÁPAGA, and MARCO A. RAMÍREZ-ARGÁEZ

In the current study a transparent water physical model was developed to study fluid flow and turbulent structure of aluminum ladles for degassing treatment with a rotating impeller and gas injection. Flow patterns and turbulent structure in the ladle were measured with the particle image velocimetry technique. The effects of process parameters such as rotor speed, gas flow rate, and type of rotor on the flow patterns and on the vortex formation were analyzed using this model, which control degassing kinetics. In addition, a comparison between two points of gas injection was performed: (a) conventional gas injection through the shaft and (b) a "novel" gas injection technique through the bottom of the ladle. Results show that the most significant process variable on the stirring degree of the bath was the angular speed of the impeller, which promotes better stirred baths with smaller and better distributed bubbles. A gas flow rate increment is detrimental to stirring. Finally, although the injection point was the less-significant variable, it was found that the "novel" injection from the bottom of the ladle improves the stirring in the ladle, promotes a better distribution of bubbles, and shows to be a promising alternative for gas injection.

DOI: 10.1007/s11663-013-9845-5

I. INTRODUCTION

ALUMINUM castings for automotive applications are commonly produced by foundry processes. The quality of the final casting depends (among other factors) on the refining stage where impurities and dissolved gases are removed from the melt.

Hydrogen is without any doubt the only and the most detrimental dissolved gas affecting the physical and mechanical properties of the aluminum castings due to the porosity created in them by this gas. However, other gases such as oxygen and chlorine form compounds with aluminum such as Al_2O_3, other oxides, and chlorides with other alloying elements. Oxygen must be prevented to reach the liquid aluminum, and then a layer of salt fluxing is added at the top surface during degassing to prevent oxidation and formation of nonmetallic inclusions.[1] Chlorine is no longer used in degassing the aluminum and so, inert gases such as Ar and N_2 are now the preferred purging gases.[2] It is important to remove hydrogen and nonmetallic inclusions from the liquid aluminum when the casting to be produced requires the highest quality standards as in the case of automobile, aeronautic, or aerospace parts. Some of the relevant nonmetallic inclusions to be removed are Al_2O_3 from oxidation, Al_4C_3 (aluminum carbides form primary aluminum production), inclusions coming from the refractory-lining materials (C, SiO_2, or CaO), or if the alloy contains Mg, magnesium oxides, or spinels (MgO, $MgAl_2O_4$). Also chlorides ($MgCl_2$, NaCl, $CaCl_2$, *etc.*), borides and fluxing salt are part of these nonmetallic inclusions to be removed from aluminum alloy baths.[3] Inert gas injection in an aluminum ladle through an impeller–injector is the most efficient technology employed in industry with the aim of refining aluminum by eliminating nonmetallic inclusions and by removing dissolved gases which are detrimental for the physical and mechanical properties of the final product.

Although earlier studies by Sieverts,[4] Ransley and Neufeld[5] and Opie and Grand[6] incorporated the fundamentals to understand the degassing process of aluminum, the first mechanical device to degas molten aluminum was designed by Szekely[7] and the rotor–injector technology has been evolving since then. Although the process is efficient, the governing phenomena are still to be understood. Physical models have been used for the analysis of aluminum degassing by the impeller–injector technique because of the opacity of aluminum and because of the high-temperature conditions prevailing during operation which prevent us from

EUDOXIO RAMOS GÓMEZ, formerly Graduate Student in Materials Science and Engineering Department, Facultad de Química, UNAM, Edificio "D", Circuito de los Institutos s/n, Cd. Universitaria, C.P. 04510, Mexico, DF, Mexico, is now Numerical Simulation Consultant with the Cavendish Mexico, DF, Mexico. ROBERTO ZENIT, Researcher, is with the Materials Research Institute UNAM, Cd. Universitaria, CARLOS GONZÁLEZ RIVERA and MARCO A. RAMÍREZ-ARGÁEZ, Professors, are with the Materials Science and Engineering at the Metallurgical Engineering Department, Facultad de Química, UNAM, Edificio "D", Circuito de los Institutos s/n, Cd. Universitaria. Contact e-mail: marco.ramirez@unam.mx GERARDO TRÁPAGA, Professor, is with the Centro de Investigación y de Estudios Avanzados del IPN, Unidad Querétaro, Libramiento Norponiente 2000, Fracc. Real de Juriquilla, C.P. 76230, Querétaro, Mexico.

Manuscript submitted June 4, 2012.
Article published online April 11, 2013.

visualizing details of the physics involved during the refining stage. Several physical models, representing the degasification of aluminum using the rotating impeller–injector technique, have been built by using water and air representing aluminum and inert gas, respectively, by meeting geometric, dynamic, and kinematic similarities, although it was claimed that this last criterion is impossible to satisfy employing water.[8] By means of the physical models, several aspects have been explored, such as the relative performances of different designs and sizes of impellers,[9] gas holdup and ascending velocity of the bubbles,[10] vortex formation,[11] and gas removal kinetics through the removal of dissolved oxygen from water by purge of argon, nitrogen, or mixtures of this two gases,[12–14] or through the CO_2 absorption in a NaOH aqueous solution.[15] In some investigations, the measurement of the torque of the shaft was used to determine the mechanical energy supplied into the ladle,[16] and finally, in a previous study, the particle image velocimetry (PIV) technique was used to characterize a small-scale physical model to obtain fluid flow patterns and turbulence in a conventional gas injection through the shaft.[17]

In the current study, fluid flow patterns and turbulent structure of a full-scale water physical model of an aluminum ladle equipped with the rotor–injector technique were determined by measurements using a PIV technique. The effect of process and design variables, such as rotor speed, gas flow rate, and a novel point of injection from the bottom of the ladle (proposed in the current study) on the fluid dynamics and vortex size in the model were determined to analyze indirectly degassing kinetics and to validate a mathematical model developed in another study.[18]

II. EXPERIMENTAL PROCEDURE

A full-scale water physical model of an industrial batch degassing unit was made of acrylic. Dimensions of the cylindrical ladle are 0.5 m in diameter with height of liquid of 0.55 m. Rotor diameter is 0.25 m. The rotor's middle line is always located at a depth of 18 cm from the ladle bottom (Figure 1(a)). The model was designed to fulfill geometric, kinematic, and dynamic similarities (Reynolds numbers are equal in both the model and industrial system). The model has a steel structure to provide mechanical stability to an electric engine that provides variable angular speed to a shaft and a commercial rotor made of Nylamid®. Gas can be injected conventionally through the shaft or by a novel point of injection at the bottom of the ladle (Figure 1(a) to see specific location of the novel gas injection point), and its flow rate is controlled by a flow meter. Flow patterns and turbulence were determined by a PIV system using fluorescent particle tracers of polyamide (50 μm in diameter) coated with rhodamine B to avoid light reflection by the gas bubbles. Four transversal planes at different heights (9, 18, 30, and 39 cm from the bottom) and a central longitudinal plane were selected to measure the fluid dynamics (Figure 1(b)). For the transversal planes, the laser plane was aligned parallel to the base of the ladle; while for the longitudinal plane, it was aligned parallel to the radial coordinate of the ladle. Owing to the size of the longitudinal plane, two overlapped shots were necessary to cover the whole domain, while for the transversal views, only one shot was needed to cover the quarter of the system required to get the flow pattern due to the angular symmetry of the system. A New Wave Research laser system model

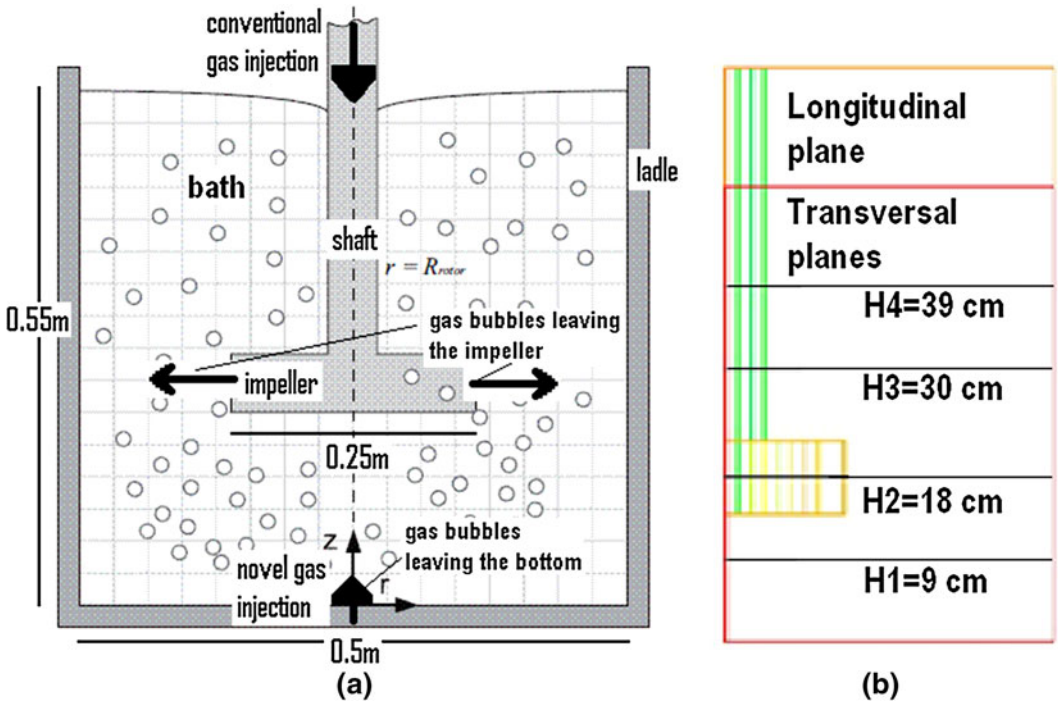

Fig. 1—(*a*) Schematic of the ladle showing dimensions and points of gas injection. (*b*) Longitudinal and transversal planes where PIV measurements were performed.

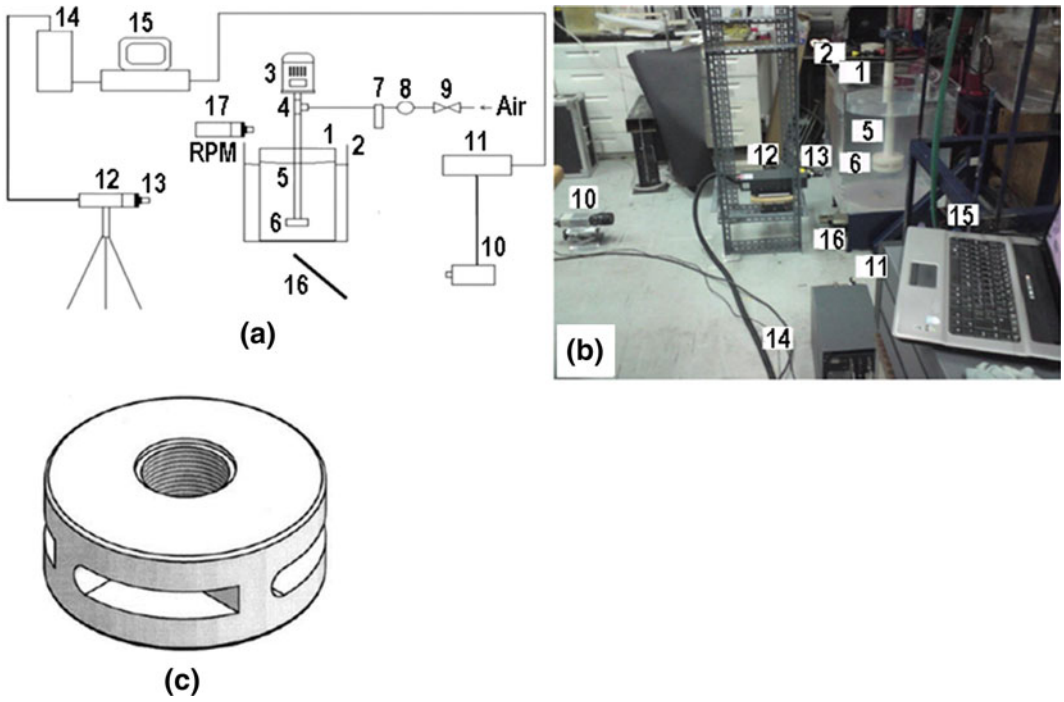

Fig. 2—(*a*) Schematic of experimental setup. (*b*) Photograph of the experimental setup. (*c*) Commercial impeller used in this work. 1: Cylindrical ladle of acrylic, 2: External acrylic recipient to avoid distortion, 3: Electric engine, 4: Rotating joint, 5: Shaft of Nylamid, 6: Impeller of Nylamid, 7: Flow meter, 8: Pressure regulator, 9: Valve, 10: Digital camera CCD, 11: Synchronizer, 12: Laser generator, 13: Optic arrangement to create the laser plane, 14: Source power to generate the laser, 15: Computer, 16: Mirror aligned 45 deg from camera view, 17: Digital tachometer.

Table I. Process and Variables for Each Experiment

Experiment Number	Injection Point	Gas Flow Rate (L/min)	Impeller Angular Speed (rpm)	Nomenclature
1	no gas injection	0	290	L
2	no gas injection	0	573	H
3	conventional	10	290	L10conv
4	conventional	40	290	L40conv
5	conventional	10	573	H10conv
6	conventional	40	573	H40conv
7	novel	10	290	L10novel
8	novel	40	290	L40novel
9	novel	10	573	H10novel
10	novel	40	573	H40novel

SOLO III was synchronized to a high speed Kodak Mega Plus camera model ES 1.0 (DANTEC Systems) through a conventional Personal Computer. Acquisition and analysis conditions were 50 pairs of photographs, each pair at intervals of every 500 ms, time between expositions was 1000 μs, with a total time of 25 seconds for every experiment. To perform the image analysis, the cross-correlation method with integration areas of 32×32 pixels was used, equivalent to a frame of 6×6 mm with an overlap of 50 pct. Every set of conditions was run and measured by triplicate, and these data were statistically analyzed to obtain a single-velocity vector map for each plane and for each test.

Images captured by the camera were processed using the software "Flow Manager v 4.6", and all vector components and plots of flow patterns were determined by processing data using the software "Matlab v 7.0". Figure 2(a) and (b) presents the scheme and a photograph of the experimental setup, respectively. A process analysis was carried out to estimate the effects of two injection points (conventional injection through the shaft and a novel injection from the ladle bottom), two rotor speeds (290 and 573 rpm), and three gas flow rates (0, 20, and 40 L/min), through a design of experiments. Table I shows 10 experiments with the specific conditions used. Figure 2(c) shows the commercial rotor used in the current study.

III. RESULTS AND DISCUSSION

A. *Qualitative Determination of Size and Distribution of Bubbles*

Figure 3 shows photographs of the model using the commercial standard impeller. Conditions are labeled

on each photo. These pictures give a qualitative estimation of the bubble size and its distribution in the ladle. High rotor speed promotes smaller bubbles being better distributed in the ladle than the low speeds. At high rotor speed, bubbles sizes are small with both gas flow rates of 40 and 10 L/min, but the concentration of bubbles is greater with 40 L/min than with 10 L/min. At low rotor speeds, bubble concentrations are similar regardless of the gas flow rate, but greater bubbles sizes are observed with 40 L/min than with 10 L/min. These big bubbles are concentrated at the center of the ladle, and they ascend vertically toward the free surface indicating the predominance of the buoyancy forces over the drag forces and reducing the residence time of the bubble, which is detrimental to the degassing kinetics. Figure 3 shows that the novel gas injection promotes smaller and better distributed bubbles at low- and high-rotating speeds with both gas flow rates of 40 and 10 L/min. With novel gas injection, the presence of the bubbles reaches regions closer to the reactor wall than in the case of conventional injection. An increase in the rotor speed gives more mechanical energy which is used to break the gas flow into small bubbles that are ejected from the impeller and dispersed through the entire ladle. These tiny bubbles follow trajectories close to those of the liquid flow patterns since drag forces exerted from the liquid overcome buoyancy forces, increasing residence time of the bubbles, which it is good for degassing.

B. *Velocity Fields*

Figures 4 through 7 show the velocity fields of the liquid at transversal planes (r–θ planes) located at heights of 9, 18, 30, and 39 cm, respectively. Every plot presents the experimental conditions. The liquid velocity profile depends on the radial and axial positions. For the transversal plane located 9 cm from the bottom, high velocities were measured with a maximum located at 5 cm from the radius of the rotor regardless of the operational conditions. For the plane located at the level of the rotor (18 cm from ladle bottom), magnitudes of the liquid velocity decrease, and the velocity profile is flatter than velocities profiles measured at 9 cm from bottom. These two planes present velocity vectors with both radial and angular components of the velocity, with the angular component being dominant of the flow field by the momentum transferred from the rotating impeller to the liquid. At the plane located 30 cm from bottom, the rotor acted as an obstacle for the camera, so that the entire radial profile was not available, but a flat radial velocity profile is observed as well as the absence of the radial component of the velocity; the motion is mainly in the angular direction. The magnitude of the velocities is comparable to those of the deeper planes (9 and 18 cm from bottom). In the plane located at an axial position of 39 cm from the bottom and closer to the free surface, the presence of the vortex and the rotor obstacle prevents a full measurement of the liquid velocity along the entire radius, but it can be observed that smaller liquid velocity magnitudes are present. In

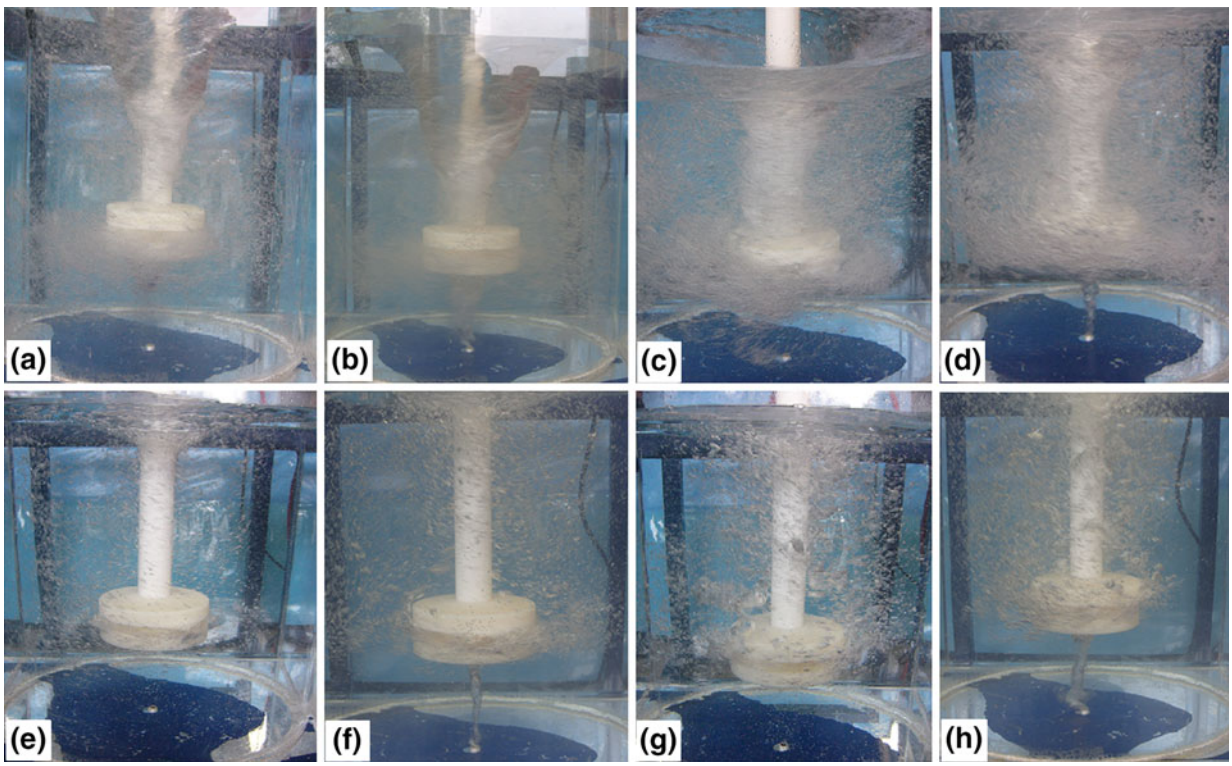

Fig. 3—Photographs showing qualitatively gas bubble sizes, bubble distribution, and vortexes. (*a*) 573 rpm, 10 L/min, conventional, (*b*) 573 rpm, 10 L/min, novel, (*c*) 573 rpm, 40 L/min, conventional, (*d*) 573 rpm, 40 L/min, novel, (*e*) 290 rpm, 10 L/min, conventional, (*f*) 290 rpm, 10 L/min, novel, (*g*) 290 rpm, 40 L/min, conventional, (*h*) 290 rpm, 40 L/min, novel.

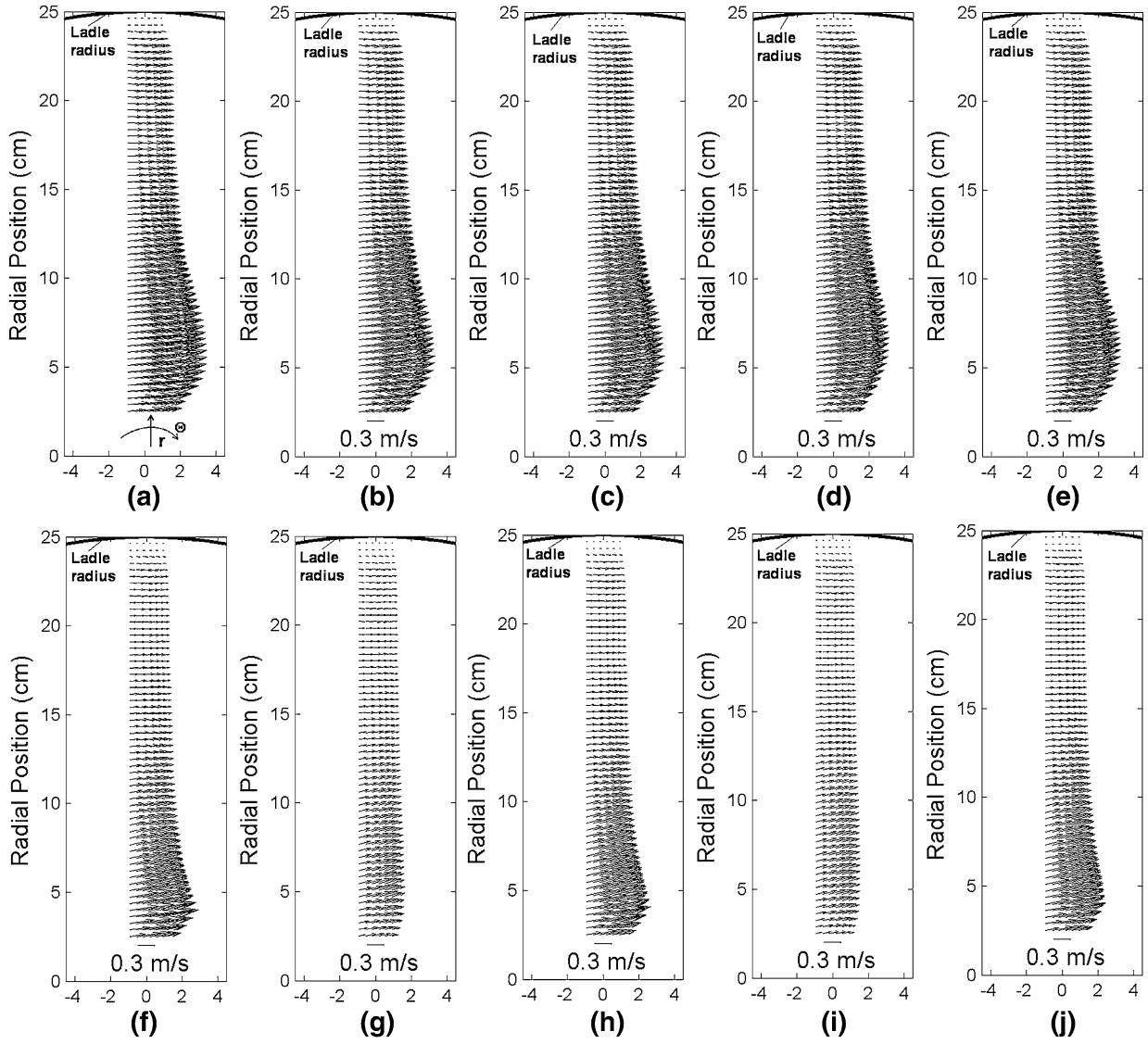

Fig. 4—Liquid-velocity vector plots measured at a r–θ plane located at a height of 9 cm from the ladle bottom (below the impeller) under several operating conditions. (*a*) 573 rpm no gas injection, (*b*) 573 rpm, 10 L/min, conventional, (*c*) 573 rpm, 10 L/min, novel, (*d*) 573 rpm, 40 L/min, conventional, (*e*) 573 rpm, 40 L/min, novel, (*f*) 290 rpm, no gas injection, (*g*) 290 rpm, 10 L/min, conventional, (*h*) 290 rpm, 10 L/min, novel, (*i*) 290 rpm, 40 L/min, conventional, (*j*) 290 rpm, 40 L/min, novel. Reference vector of 0.3 m/s.

general, an increase of the angular speed of the impeller promotes greater liquid velocities due to the higher momentum transfer from the impeller to the liquid. Maximum velocities are obviously found to be close to the impeller and shaft. As gas flow rate is increased, liquid velocities decrease, promoting a less-agitated bath regardless of the gas injection point and the impeller angular speed. This is because the gas bubbles inhibit the contact between the impeller and the liquid since the bubbles form a layer of gas in between the solid impeller and the liquid, which reduces the momentum transfer. The novel injection technique promotes a better stirred bath at low angular speeds than the conventional gas injection, while at high angular speed of the impeller, both injections give similar results in terms of liquid velocity profiles and magnitudes. Angular momentum transferred from the impeller to the liquid improves axial momentum transfer from the ascending gas bubbles to the liquid, resulting in a bath with a flow pattern predominating in the angular direction. Although the flow is 3D, the angular component of velocity dominates the flow field structure. Only at low rotor speeds and high flow rates, big bubbles concentrated at the center promote more axial momentum than angular momentum, *i.e.*, bad conditions for degassing.

Figure 8 shows velocity profiles at the longitudinal central plane of the ladle. Owing to the large size of the system, two shots were taken to cover the entire domain. This plane does not show the main contribution of the liquid velocity which is azimuthally; however, this plane shows the 3D nature of the flow, since radial and axial components of the velocity are present. Although it is difficult to clearly identify flow patterns because of the random liquid motion characteristic of a turbulent flow

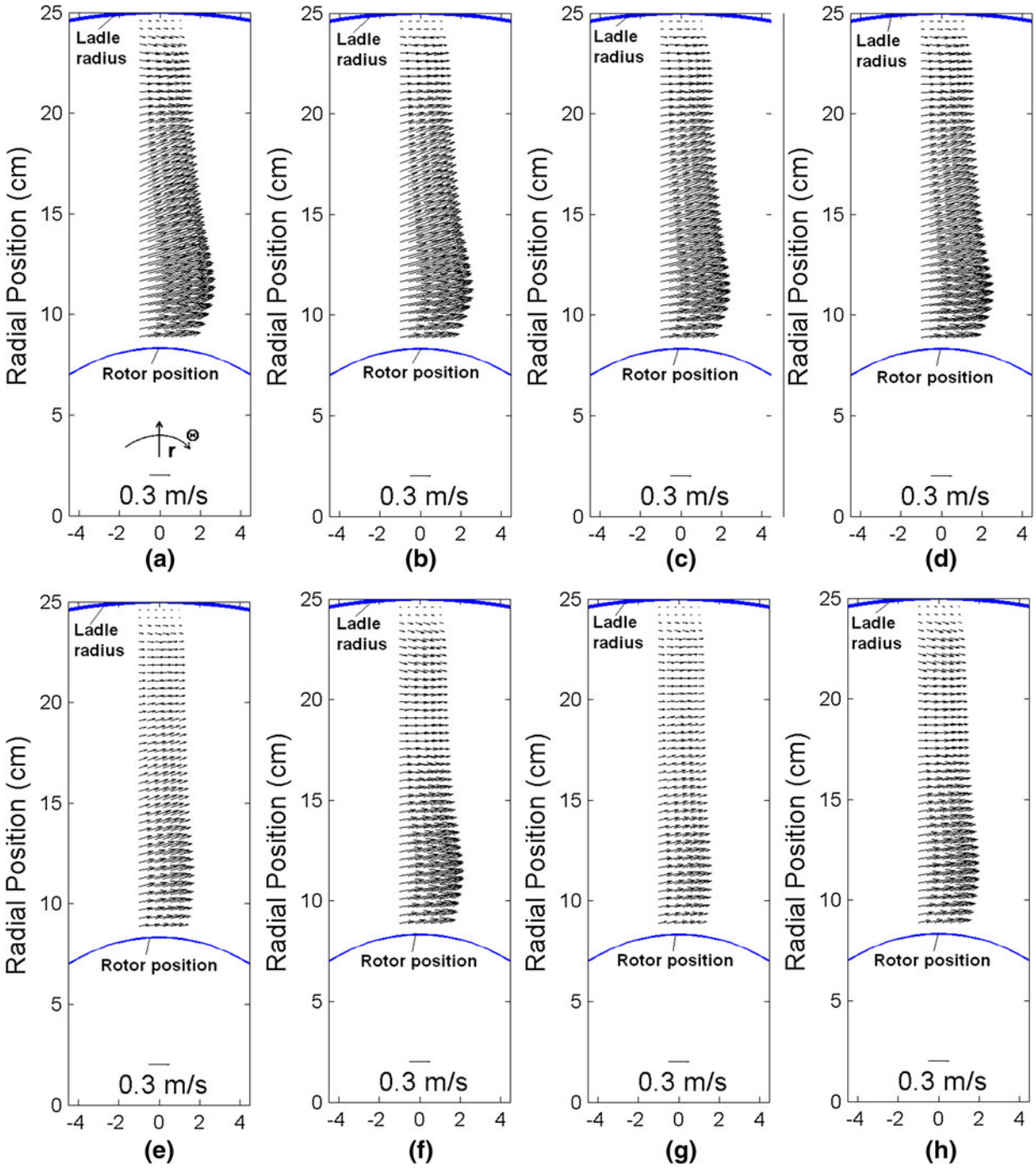

Fig. 5—Liquid-velocity vector plots measured at a r–θ plane located at a height of 18 cm from the ladle bottom (at the level of the impeller) under several operating conditions. (*a*) 573 rpm, 10 L/min, conventional, (*b*) 573 rpm, 10 L/min, novel, (*c*) 573 rpm, 40 L/min, conventional, (*d*) 573 rpm, 40 L/min, novel, (*e*) 290 rpm, 10 L/min, conventional, (*f*) 290 rpm, 10 L/min, novel, (*g*) 290 rpm, 40 L/min, conventional, (*h*) 290 rpm, 40 L/min, novel. Reference vector of 0.3 m/s.

(although the velocity vectors plotted are time averaged), two circulating regions can be defined: (a) one is located at the lower part of the ladle conducting a counterclockwise circulation starting from the fluid being pumped from the bottom of the impeller, which leaves the impeller in radial direction toward the ladle lateral wall, then goes down to the bottom wall, and finally, returns to the impeller; (b) a circulation loop in the clockwise direction starting from the impeller and extending to the lateral wall in radial direction, then going up to the free surface turning to the center of the ladle, and going down back to the impeller. Certainly, these circulations are difficult to distinguish from the plots of Figure 8, but from mathematical model results, the circulations are clearly defined.[18] These circulations are formed at the bottom of the impeller, where a low

pressure is created, which draws fluid that is ejected radially. Centrifugal forces that push liquid toward the ladle wall are counterbalanced by the radial pressure gradient, which in turn creates the vortex at the free surface. When the gas flow rate is high and the rotor speed is low, the upper circulation loop disappears since the flow is vertically moved by the drag from the big bubbles located at the center of the ladle. Some features can be observed, such as the increment in the magnitude of the liquid velocity with an increase in angular speed of the rotor, and at low rotor speeds and high gas flow rate, there is dominant upward motion of the liquid due to the drag exerted from the bubbles to the liquid. This figure also shows the presence and size of the vortex at the free surface (the approximate vortex shape is labeled in every plot of Figure 8), showing an increase in the vortex size with the increase in rotor speed and a decrement in this size of the vortex with an increase in the gas flow rate, while the point of gas injection has no effect on the vortex size.

C. *Radial Velocity and Turbulent Profiles*

Previous vector plots of the liquid velocity provide a qualitative picture of the fluid dynamics in the ladle, but for a quantitative analysis, dimensionless velocity and turbulent kinetic energy radial profiles were computed. Dimensionless velocity, v^*, was computed with Eq. [1], where u_{rotor}, r_{ext}, and rpm are rotor speed, ladle radius and angular velocity of the impeller respectively, while u_θ and u_r are angular and radial components of the velocity.

$$v^* = \frac{\overrightarrow{u}}{u_{\text{rotor}}} = \frac{\sqrt{u_\theta^2 + u_r^2}}{2\pi r_{\text{ext}} \text{rpm}} \quad [1]$$

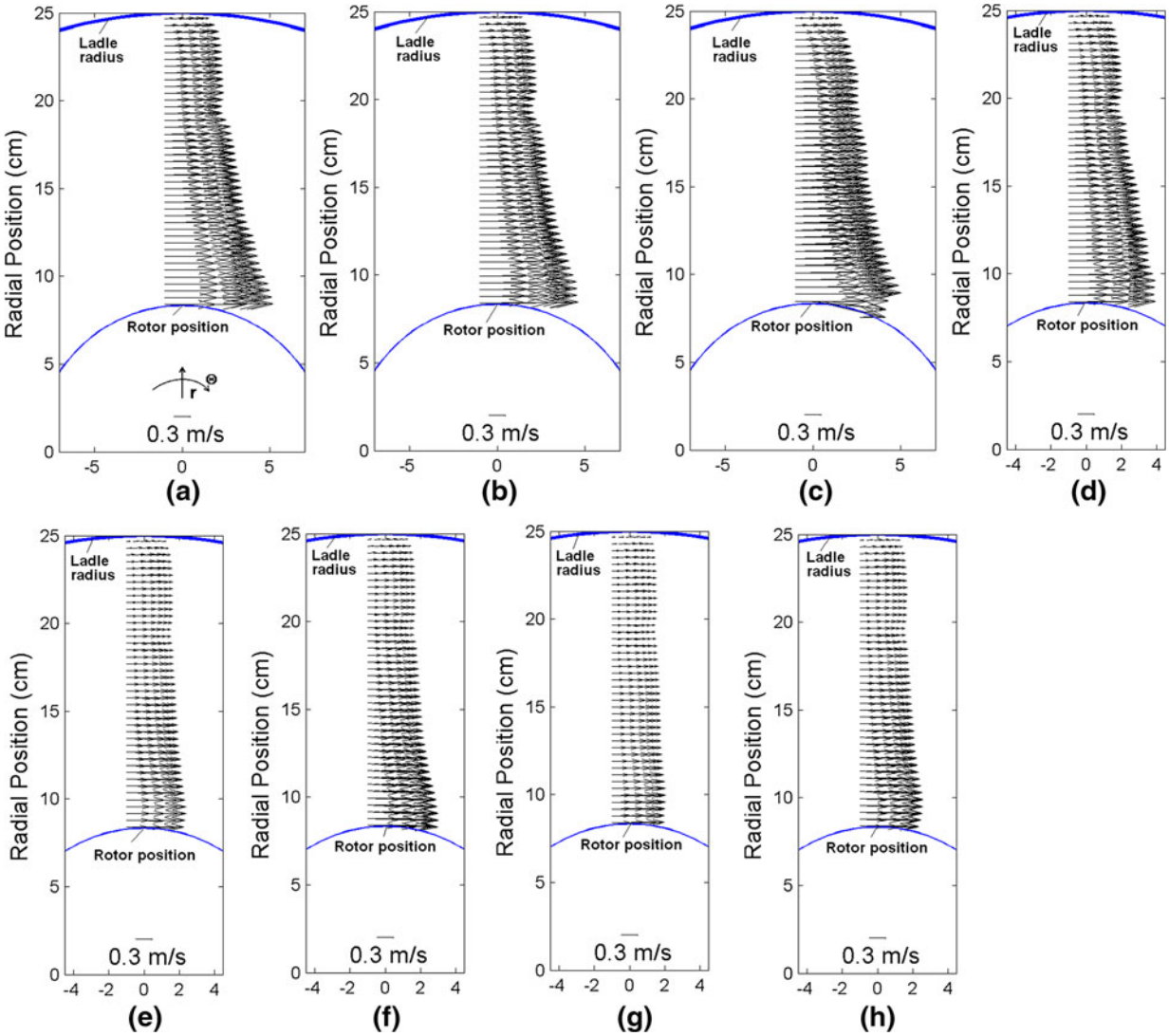

Fig. 6—Liquid-velocity vector plots measured at a r–θ plane located at a height of 30 cm from the ladle bottom (above the level of the impeller) under several operating conditions. (*a*) 573 rpm, 10 L/min, conventional, (*b*) 573 rpm, 10 L/min, novel, (*c*) 573 rpm, 40 L/min, conventional, (*d*) 573 rpm, 40 L/min, novel, (*e*) 290 rpm, 10 L/min, conventional, (*f*) 290 rpm, 10 L/min, novel, (*g*) 290 rpm, 40 L/min, conventional, (*h*) 290 rpm, 40 L/min, novel. Reference vector of 0.3 m/s.

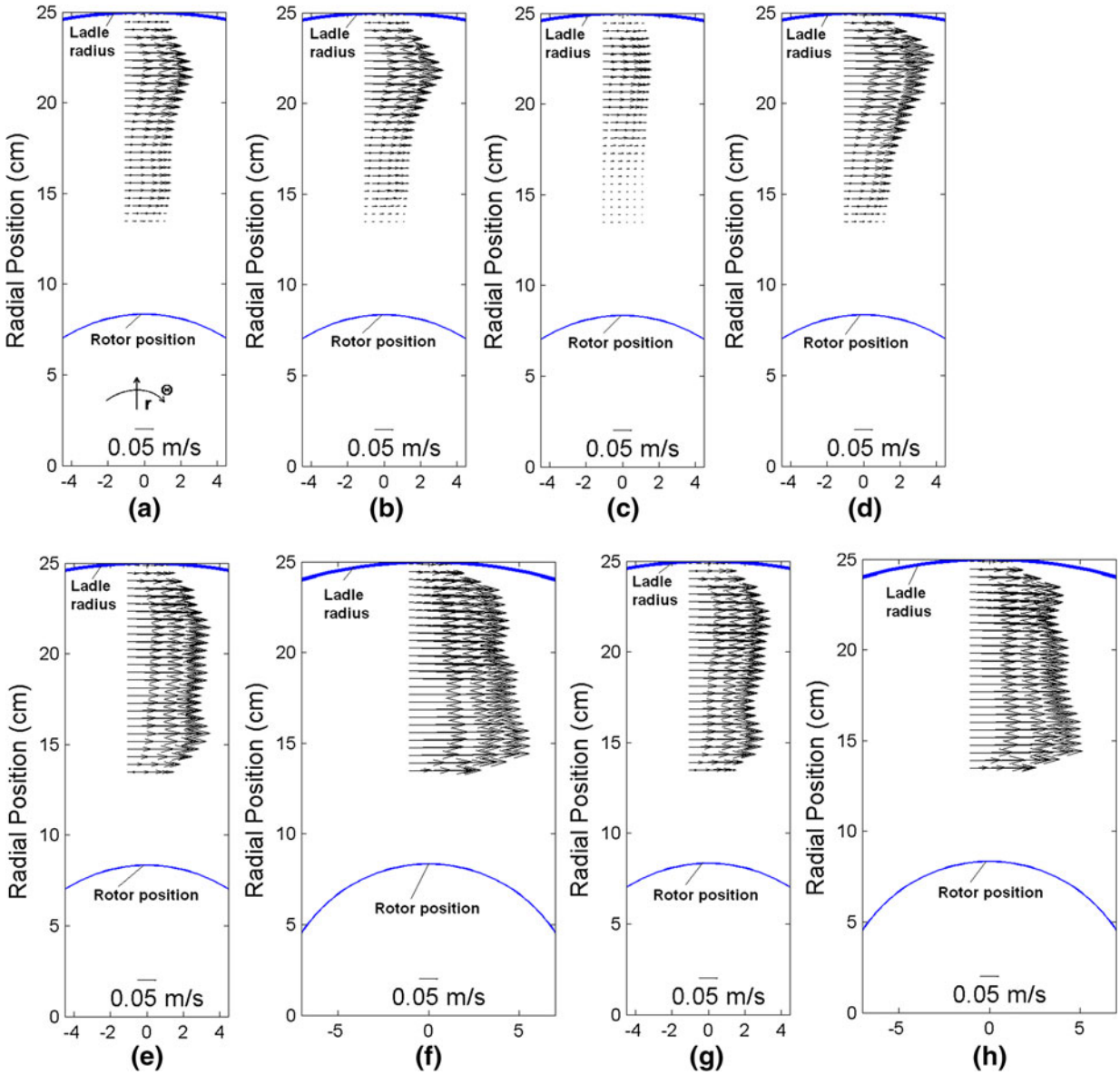

Fig. 7—Liquid-velocity vector plots measured at a r–θ plane located at a height of 39 cm from the ladle bottom (at the free surface) under several operating conditions. (*a*) 573 rpm, 10 L/min, conventional, (*b*) 573 rpm, 10 L/min, novel, (*c*) 573 rpm, 40 L/min, conventional, (*d*) 573 rpm, 40 L/min, novel, (*e*) 290 rpm, 10 L/min, conventional, (*f*) 290 rpm, 10 L/min, novel, (*g*) 290 rpm, 40 L/min, conventional, (*h*) 290 rpm, 40 L/min, novel. Reference vector of 0.05 m/s.

Turbulence of the liquid phase improves the mixing and mass exchange between gas and liquid, thus improving degassing kinetics. Turbulence is represented by the turbulent kinetic energy and by the turbulent intensity. Turbulent kinetic energy, k and dimensionless turbulent kinetic energy, k^*, can be obtained with Eqs. [2] and [3], where u'_θ and u'_r are the angular and radial fluctuating components of the velocity.

$$k = \frac{u_\theta'^2 + u_r'^2}{2} \quad [2]$$

$$k^* = \frac{u_\theta'^2 + u_r'^2}{2u_{rotor}^2} = \frac{u_\theta'^2 + u_r'^2}{2(\pi r_{ext} \mathrm{rpm})^2} \quad [3]$$

IT is the turbulent intensity, and IT^* is dimensionless turbulent intensity, which are functions of the turbulent kinetic energy (Eqs. [4] and [5]).

$$IT = \frac{\sqrt{2/3k}}{\overrightarrow{u}} \quad [4]$$

$$IT^* = \sqrt{2/3k^*} \quad [5]$$

Figure 9(a) shows dimensionless velocity radial profiles, and Figure 9(b) shows the dimensionless turbulent intensity radial profile, both measured at an axial position of 30 cm from the bottom. Plots present results under different operational conditions of gas flow rate, rotor

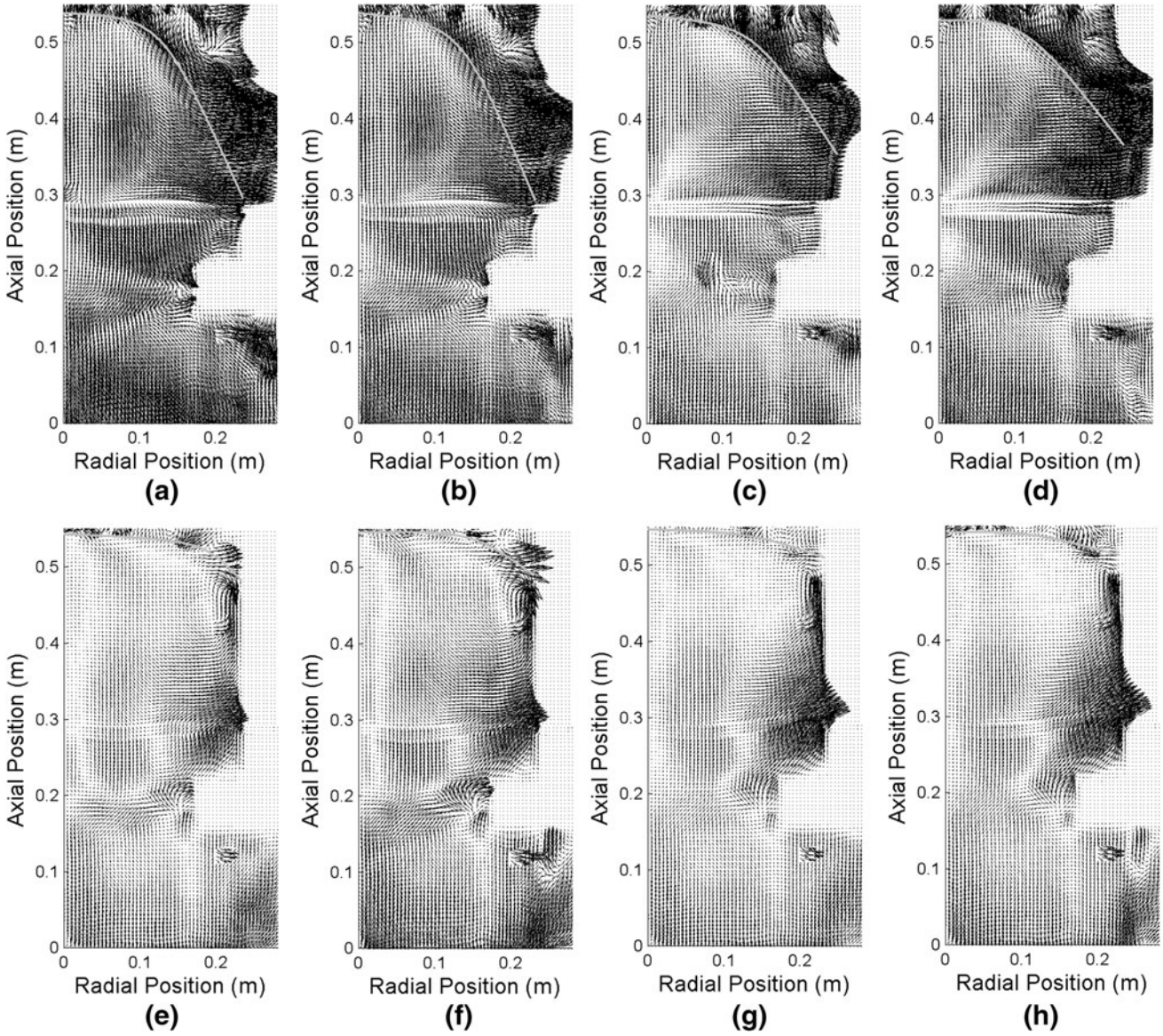

Fig. 8—Liquid-velocity vector plots measured at a *r–z* plane located at the center of the ladle under several operating conditions. (*a*) 573 rpm, 10 L/min, conventional, (*b*) 573 rpm, 10 L/min, novel, (*c*) 573 rpm, 40 L/min, conventional, (*d*) 573 rpm, 40 L/min, novel, (*e*) 290 rpm, 10 L/min, conventional, (*f*) 290 rpm, 10 L/min, novel, (*g*) 290 rpm, 40 L/min, conventional, (*h*) 290 rpm, 40 L/min, novel. Reference vector of 0.3 m/s.

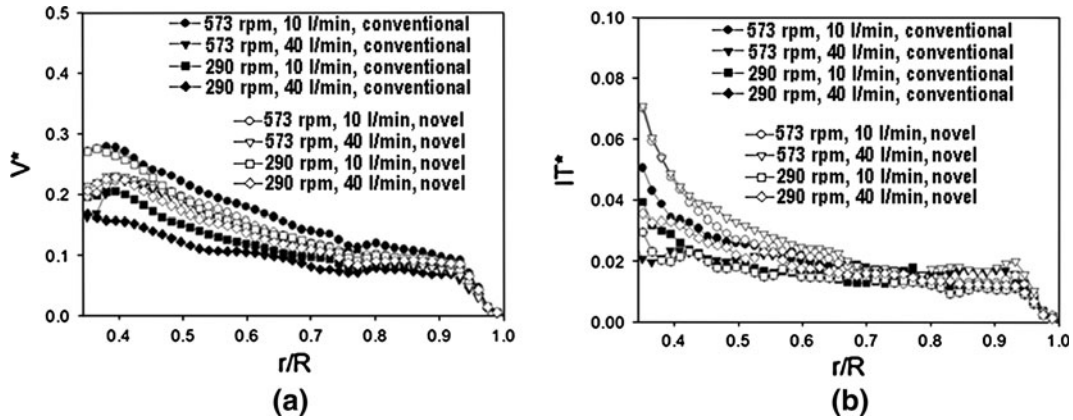

Fig. 9—(*a*) Dimensionless velocity radial (*V**) profile at a height of 30 cm from the bottom of the ladle (above the impeller). (*b*) Dimensionless turbulent intensity (*IT**) radial profile at a height of 30 cm from the bottom of the ladle (above the impeller).

speed, and point of gas injection. It is confirmed that velocities decrease with an increment in the gas flow rate. At low rotor speed, the novel injection provides more agitation than the conventional injection, which results in a more efficient momentum transfer between the rotor and liquid in the novel gas injection than the conventional gas injection. It is also interesting to note that the velocity profiles obtained with the novel gas injection technique are almost the same regardless of the gas flow rate or the rotor speed. Since the dimensionless velocity are obtained by dividing them over the rotor speed, similar velocities profiles mean that velocities are directly proportional to the rotor speed. The contrary happens for the conventional injection, where the profiles are not the same and a negative effect can be observed on the stirring of the bath when the gas flow is increased.

Analyzing the turbulence intensity, it is clear that the presence of gas bubbles increase turbulence due to the extra turbulence produced by the bubbles ascending motion through the liquid. Also, an increase in the rotor speed increases the inertial forces in the liquid, and turbulence is increased. The plot shows a dimensionless parameter normalized by dividing the turbulence over the rotor velocity, *i.e.*, equal dimensionless turbulence intensities for different rotor speeds mean a proportional increase in turbulence with an increase in rotor speed. However, turbulence is larger at high rotor speeds for the novel technique than the conventional technique, but at low rotor speeds both injection points show similar turbulences.

IV. CONCLUSIONS

The flow field structure shows a predominant angular motion of the liquid due to the momentum transferred by the impeller to the liquid, but the flow patterns show a complex 3D turbulent regime with two liquid circulations loops in the longitudinal plane-one counterclockwise in the lower part of the ladle, and the other clockwise in the upper part of the ladle, which is broken if the gas flow rate is high enough to promote vertical flow of the liquid by overcoming the angular momentum of the rotor by the drag of the bubbles ascending by buoyancy. Centrifugal forces from the high-speed rotating impeller are counterbalanced by radial gradient pressures that explain vortex formation and the pumping effect of the impeller.

An increment in the rotor speed increases stirring in the liquid, and turbulence intensity; it promotes smaller and better-distributed bubbles in the ladle with higher residence times, which are good features for degassing, but results in bigger vortices. The mechanical energy of the rotating impeller is used to transfer angular momentum to the liquid, break the gas flow into a small bubbles, and to disperses these bubbles through the entire ladle.

The gas flow rate increases the gas hold up in the ladle, decreases vortex sizes, and turbulence, but it decreases the stirring of the liquid since the gas contacting the impeller reduces the momentum transfer from the impeller to the liquid.

The novel gas injection from the bottom improves the stirring of the bath (both velocities and turbulence intensity) and promotes smaller and better distributed bubbles at low- and high-rotating speeds.

ACKNOWLEDGMENTS

Marco A. Ramírez-Argáez is greatful to Cinvestav for the support provided whole writing this article during his sabbatical year at Cinvestav, Unidad Querétaro.

REFERENCES

1. M. Maniruzamman and M. Makhlouf: *Phase Separation Technology in Aluminum Melt Treatment, A Monograph*, AFS, Des Plaines, IL, 2000.
2. R.D. Peterson and P.A. Wells: In *Light Metals 1992*. The Minerals, Metals & Materials Soc., Warrendale, PA, 1992, vol. 121, pp. 1023–29.
3. B. Prillhofer, H. Antrekowitsch, H. Böttcher, and P. Enright: in *Light Metals 2008*. The Minerals, Metals & Materials Soc., Warrendale, PA, 2008, vol. 2008, pp. 603–08.
4. A. Sieverts: *Z. Metallkunde*, 1929, vol. 21, pp. 37–46.
5. C.E. Ransley and H. Neufeld: *J. Inst. Metals*, 1947, vol. 74, pp. 559–620.
6. W.R. Opie and W.J. Grant: *Trans. AIME*, 1950, vol. 188, pp. 1237–41.
7. A.G. Szekely: US Patent 3,870,511, 1975.
8. J.F. Grandfield, D.W. Irwin, S. Brumale and C.J. Simansen: in *Light Metals 1990*. The Minerals, Metals & Materials Soc., Warrendale, PA, 1990.
9. M. Nilmani, P.K. Thay, and C.J. Simensen: *Light Metals 1992*. The Minerals, Metals & Materials Soc., Warrendale, PA, 1992, vol. 121, pp. 939–46.
10. Y. Ohno, D.T. Hampton, and A.W. Moores: *Light Metals 1993*. The Minerals, Metals & Materials Soc. (TMS), Warrendale, PA, 1993, vol. 122, pp. 915–21.
11. M. Nilmani, P.K. Thay, C.J. Simansen, and D.W. Irwin: *Light Metals 1990*. The Minerals, Metals & Materials Soc., Warrendale, PA, 1990, vol. 119, pp. 747–54.
12. F. Boeuf, M. Rey, and E. Wuilloud: in *Light Metals 1993*. The Minerals, Metals & Materials Soc., Warrendale, PA, 1990, vol. 122, pp. 927–32.
13. M. Saternus and J. Botor: *Metalurgija*, 2009, vol. 48, pp. 175–79.
14. S.T. Johansen, S. Grådahl, P. O. Grøntvedt, P. Tetlie, R. Gammelsæter, K. Venås, P. Skaret, E. Myrbostad and B. Rasch: *Light Metals 1997*. The Minerals, Metals and Materials Society, Warrendale, PA, 1997, vol. 126, pp. 663–66.
15. M. Guofa, Q. Shouping, L. Xiangyu, and N. Jitai: *Mater. Sci. Eng. A*, 2009, vol. 499, pp. 195–99.
16. A. Fjeld, S. Edussuriya, J.W. Evans, and A. Mukhopadhyay: *Light Metals 2005*. The Minerals, Metals and Materials Soc., Warrendale, PA, 2005, vol. 34, pp. 963–68.
17. J.L. Camacho-Martínez, M.A. Ramírez-Argáez, R. Zenit, A. Juárez-Hernández, J.D. Oscar Barceinas, and G. Trápaga: *Mater. Manuf. Processes*, 2010, vol. 25, pp. 1–11.
18. E. Ramos-Gómez, R. Zenit, C. González-Rivera, G. Trapaga, and M. Ramírez-Argáez: *Metall. Mater. Trans. B*, 2013, vol. 44B, pp. 423–35.